Nonlinear Simulations of Jupiter's 5-Micron Hot Spots

Adam P. Showman[1]* and Timothy E. Dowling[2]*

Large-scale nonlinear simulations of Jupiter's 5-micron hot spots produce long-lived coherent structures that cause subsidence in local regions, explaining the low cloudiness and the dryness measured by the Galileo probe inside a hot spot. Like observed hot spots, the simulated coherent structures are equatorially confined, have periodic spacing, propagate west relative to the flow, are generally confined to one hemisphere, and have an anticyclonic gyre on their equatorward side. The southern edge of the simulated hot spots develops vertical shear of up to 70 meters per second in the eastward wind, which can explain the results of the Galileo probe Doppler wind experiment.

The Galileo probe's in situ measurements of composition, winds, and temperature within Jupiter's atmosphere raise questions about conditions below the planet's outer cloud deck at 0.7 bars (1 bar = 10^5 Pa). The observations showed that water was just 0.03 times solar at 11 bars and 0.3 times solar at 19 bars, H_2S surged from 0.3 times solar at 8 bars to 2.5 times solar at 16 bars, and NH_3 increased from less than 2 to about 4 times solar from 1 to 10 bars (*1–4*). The low water abundance contradicts formation models, meteorological studies, and infrared (IR) retrievals that have suggested abundances up to 10 times solar below the clouds (*5–12*). Furthermore, although the measured abundances of NH_3 and H_2S are consistent with expectations at pressures exceeding 10 and 16 bars, respectively, the diminished abundance of these species from 1 to 10 bars is surprising. Condensation can only remove NH_3, H_2S, and water at pressures less than 0.7, 2, and 5 bars, respectively, suggesting that the height-dependence at greater pressures results from dynamics. The winds measured by the Galileo probe are also intriguing: Doppler tracking of the probe radio signal indicated eastward winds of 90 m s^{-1} near 0.5 bars, increasing to 180 m s^{-1} at 5 bars, and remaining nearly constant down to the end of the probe trajectory at 22 bars (*13*). The extent to which this wind shear is representative—of the whole planet, or just to local regions such as eastward jets (*14*), or only to the Galileo probe site—is unknown.

Understanding the relevance of the probe data for Jupiter's global state is complicated by the fact that the probe entered one of Jupiter's most unusual areas, a 5-μm hot spot (Fig. 1) (*15*). Hot spots are local equatorial regions that cover just 0.1 to 0.5% of Jupiter's area but dominate its thermal emission to space at 5-μm wavelength (*16*). This emission emanates from pressures as deep as 8 bars, suggesting that these spots are depleted in cloud abundance and water vapor relative to other locations on Jupiter (*17–20*). Several authors have suggested that hot spots contain downdrafts that advect dry air from above the cloud tops down to 10 bars or deeper (*21–24*). If present, such a downdraft would alter winds and temperature as well as composition, and therefore any attempt to assign global implications to Galileo probe data must begin with an understanding of hot spot dynamics.

Here, we investigate whether such regions of descending air can exist and whether their dynamics are consistent with observations. We numerically solved the fully nonlinear hydrostatic primitive equations in isentropic coordinates using the Explicit Planetary Isentropic Coordinate (EPIC) finite-difference model (*25*). The initial zonal wind versus latitude is taken from Voyager cloud-tracking observations (*26*) and assumed to be constant in height. The initial pressure field is in gradient-wind balance with these winds. The initial temperature profile is idealized to be isothermal at 110 K at pressures less than 200 mbar and to have a constant Brunt-Vaisala frequency at greater pressures (*27*); we use 0.005 s^{-1}, roughly the value expected if Jupiter has a few times solar water with the stabilizing effect of latent heat release (*11*). Our domain extends 120° in longitude and ±40° in latitude, with periodic and channel (i.e., free-slip rigid wall) boundary conditions, respectively. The nominal model has six layers; the top five layers are active and have initial interface pressures of 0.083, 0.24, 0.65, 1.8, and 5.0 bars (*28*), while the sixth layer represents the neutrally stratified, convectively adjusted deep interior and has fixed winds (*26*) and pressure gradients that affect the overlying layers. The standard resolution is 128 × 90 gridpoints (0.9°), which we increase to 256 × 180 (0.45°) in selected runs to verify numerical convergence. The integration freely evolves except for a small hyperviscosity to control numerical instabilities, a radiative cooling that is negligible over the time scales considered, and a sponge in the top three layers to reduce artificial reflections of upwardly propagating waves (*29*).

Because the model's coordinate surfaces are material surfaces for dry-adiabatic motions, we induce hot spots by adding local regions of high pressure, which is equivalent to deflecting material surfaces downward. The initial high-pressure anomalies are elliptical Gaussians with the functional form $\Delta p_0 \exp[-(\phi - \phi_0)^2/a^2 - (\lambda - \lambda_0)^2/b^2]$, where Δp_0 is the increase in pressure, ϕ is east longitude, λ is planetographic latitude, ϕ_0 and λ_0 are the longitude and latitude at the center of the hot spot, respectively, and a and b are the semimajor and semiminor axes, respectively, of the hot spot. Within a given simulation, the initial hot spots are all the same size, are placed at the same latitude, and are evenly spaced in longitude (*30*). The nominal amplitude, Δp_0, is zero on the top three layers and two and four times ambient pressure on layers 4 and 5, respectively, although in some

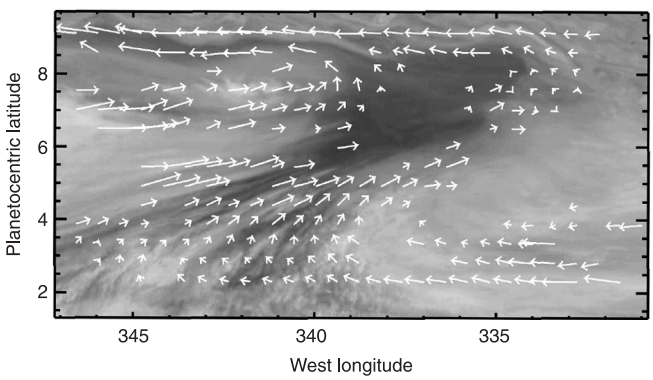

Fig. 1. A jovian 5-μm hot spot, which is the dark region, imaged in visible light by Galileo (*37*). Overlain are wind vectors in a reference frame tied to the hot spot, which moves eastward at 78 m s^{-1} relative to Jupiter's interior. The longest vectors are 50 m s^{-1}. The shortest vectors (east of the hot spot) may be noise because small cloud features there are hard to track. Hot spots are regions of low cloud abundance (hence their visible-wavelength darkness) and appear bright at 5-μm wavelengths. One degree of latitude or longitude spans 1200 km.

[1]National Research Council (NRC)/NASA Ames Research Center, Mail Stop 245-3, Moffett Field, CA 94035–1000, USA. [2]Comparative Planetology Laboratory, University of Louisville, 211 Sackett Hall, Louisville, KY 40292, USA.

*E-mail: showman@humbabe.arc.nasa.gov (A.P.S.); dowling@flolab.spd.louisville.edu (T.E.D.)

simulations, Δp_0 is set to this nominal value times a constant factor less than one. The main parameters we vary are Δp_0, wavenumber, and λ_0 of the hot spots.

When the initial pressure perturbations are placed near 8° latitude, the flow evolves to contain long-lived (100- to 200-day lifetime) coherent structures with many similarities to hot spots (Fig. 2). Time evolution indicates that the features move eastward at 35 m s^{-1}. Because the winds in the equatorial jet blow ~108 m s^{-1} at 8°N latitude, the hot spots propagate westward at 70 m s^{-1} relative to the jet. We know they are not vortices because contours of potential vorticity (a conserved variable) passing through them are not closed as they would be in the Great Red Spot, but are open streamlines that encircle the planet and exhibit a cycloidal pattern with latitudinal maxima at 6° to 8° inside hot spots and minima at 0° to 6° in the low-pressure regions between them. Consistent with observations, our simulated hot spots are generally confined to one hemisphere, although they sometimes undergo a week-long oscillation between hemispheres that is not observed (*31*).

Air flowing through the hot spots undergoes a temporary increase in pressure by up to a factor of 2. On Jupiter, this process would push dry, high-altitude air downward, forcing clouds to sublimate (thereby generating a region with high 5-μm emission) and contributing to the dryness measured by the probe. The descent is a downward stretching of vertical air columns that are statically stable; no unstable convective overturning occurs. Any layering that exists within a vertical air column is preserved during the stretching process. Our simulations can therefore explain the probe observations that NH_3, H_2S, and H_2O increased at different pressure levels: they suggest that air parcels at the initial condensation levels of NH_3, H_2S, and H_2O (near 1, 2, and 5 bars) were deflected to 8, 16, and >20 bars, respectively, because of the vertical stretching. This explains why, at the probe site, NH_3 increased from 1 to 8 bars, H_2S increased from 8 to 16 bars, and H_2O had not reached solar by the bottom of the trajectory at 20 bars. In contrast, if convectively unstable updrafts and downdrafts were present, the vertical layering would be destroyed and NH_3, H_2S, and H_2O would become vertically homogenized. Our pressure deflections are still too small, however: a complete match to the probe data requires a pressure deflection of five times or more below 5 bars, although twofold variations may be sufficient from 1 to 5 bars (*23, 32*).

Winds in a reference frame moving with the model hot spot blow from west to east through the feature (Fig. 3, top). South of the hot spot, winds move westward before turning northeast and entering the feature. This gyrelike flow is similar to the actual flow observed near a hot spot (Fig. 1). The observed flow aligns with the western half of an equatorial plume, and Hubble Space Telescope and ground-based observations show similar cloud morphology near most hot spots (*33*). Our simulated winds exit the hot spot to the east, whereas the exit position in real hot spots is less clear—winds may exit to the northwest, east, or both. Our simulations develop cross-equatorial winds southeast of the hot spot, which are not observed.

Our model develops strong vertical wind shear at the southern edge of hot spots even when little vertical shear exists elsewhere in our simulation. Poleward of 15°, the winds vary by only 2 to 10 m s^{-1} with depth. To the west of the hot spot or at its center, the winds also maintain nearly constant speeds of ~100 m s^{-1} (Fig. 3). At the northern edge, they decrease with depth. However, the Galileo probe entered the southern edge of a hot spot, and at the model hot spot's southern edge, the winds increase from about 40 m s^{-1} near 2 bars to 100 m s^{-1} in the abyssal layer below about 8 bars (Fig. 3). Because our initial winds were constant with height, this wind shear developed solely in response to the eddy structure of the hot spots. Thus, a substantial fraction of the 70 m s^{-1} shear observed by the probe from 1 to 5 bars could result from local dynamics near hot spots. The shear is associated with the existence of a stagnant region inside the gyre south of hot spots (Fig. 3, top) that overlies the faster deep flow.

The shape of our wind profile at the hot spot's southern edge is similar to that measured by the probe, but our wind profile is 50 to 70 m s^{-1} too slow at all altitudes. In a reference frame fixed to Jupiter's interior, our simulated hot spot propagation speed is also too slow by a similar speed of 65 m s^{-1} (our propagation speed is 35 m s^{-1} as opposed to the observed ~100 m s^{-1} eastward). These results suggest that our model could be improved to more closely match the Doppler-tracked winds and the hot spot propagation speed if we increased the jet speed at 8°N from 108 to 170 m s^{-1}. The possibility of

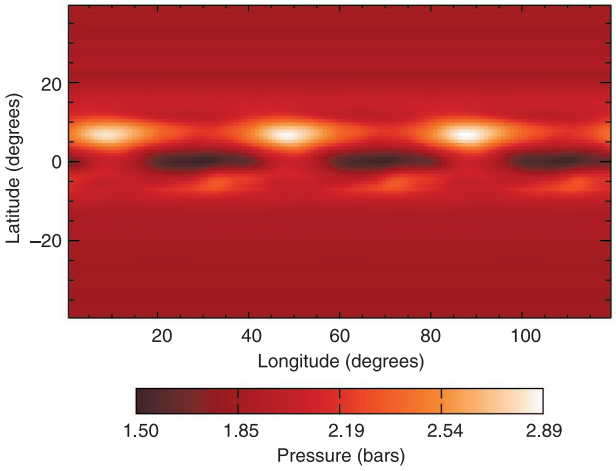

Fig. 2. Pressure on a 165 K isentrope, ranging from 2.9 bars in the bright regions to 1.5 bars in the dark regions, after 65 Earth days of evolution for a simulation with wavenumber 3 (global wavenumber 9). The bright features are the simulated hot spots. They propagate west at ~70 m s^{-1} relative to the flow. Air parcels passing through them undergo a temporary doubling of pressure, which corresponds to a downward deflection of 20 km. The adiabatic warming induced by this pressure increase would cause clouds to sublimate and produce a region bright at 5-μm wavelength.

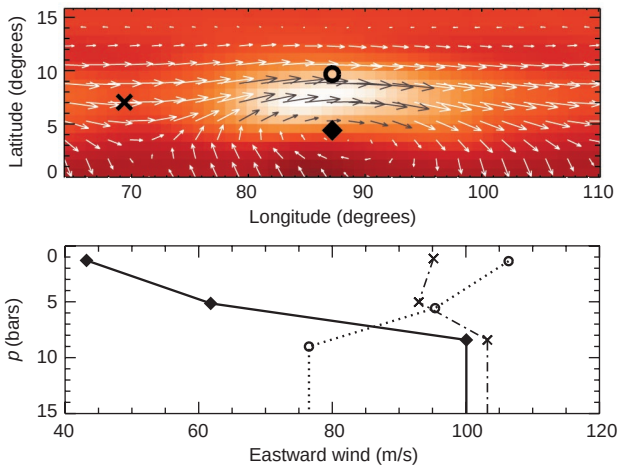

Fig. 3. (Top) Close-up image of pressure on a 165 K isentrope, overlain with wind vectors in the reference frame of the hot spot, at 64 days. In this frame, the longest arrows have speeds of 77 m s^{-1}. (Bottom) Eastward winds (relative to the interior) versus pressure at the three locations marked by the corresponding symbols shown in the above frame. Vertical shear of 60 m s^{-1} in the eastward wind develops to the south of hot spots because of their local structure. This can explain the 70 m s^{-1} shear measured by the Galileo probe at the southern edge of a hot spot and demonstrates that the planet's typical wind shear could be much smaller in magnitude than that measured at the Galileo probe site.

such a rapid jet is bolstered by the occasional sightings at 6° to 8°N of cloud features moving at speeds approaching 170 m s^{-1} (*34*), raising the possibility that the probe would have seen nearly constant winds of ~170 m s^{-1} from 1 to 20 bars had it entered the center of the hot spot. Our simulations with such a rapid jet, however, generate hot spots less coherent than those shown in Figs. 2 and 3, suggesting that a higher Δp_0 may be needed in this case.

Our hot spot propagation speeds depend on Δp_0 and zonal wavenumber. Simulations with nominal Δp_0 exhibit eastward hot spot speeds ranging from 25 to 47 m s^{-1} for global wavenumbers of 3 to 15, implying a 2 m s^{-1} increase in speed per increment in wavenumber. Simulations initialized with one-tenth the nominal Δp_0 exhibit a similar dependence on wavenumber but travel almost 30 m s^{-1} faster. (Speeds were measured over 10- to 20-day intervals at times 50 to 75 days after the simulations began.) Because the jet at 8°N is about 108 m s^{-1}, the features propagate westward relative to the jet with a speed that is faster for smaller wavenumber and higher Δp_0. Observed speeds relative to Jupiter's interior are 99.5 and 103.5 m s^{-1} eastward for global wavenumbers of 8 and 10, respectively (*16*), so our model provides a good match to the observed change in speed with zonal wavenumber. And although observed hot spots nearly advect with the zonal–mean cloud–top eastward flow at their latitude, the Galileo probe deep-wind measurement of 170 m s^{-1} suggests that real hot spots propagate westward at 70 m s^{-1} relative to the deep flow, which is similar to the propagation speed of our highest amplitude hot spots relative to the flow. The observed behavior suggests that Rossby wave dynamics control hot spot motion (*11, 16, 35*), and our simulations support this suggestion but indicate the importance of nonlinear effects in modifying the dynamics.

Our simulated hot spots remain coherent only at high Δp_0, indicating that nonlinear effects are important in maintaining them (Fig. 4). The low-amplitude hot spots are distended and change shape and amplitude over 22-hour time scales, suggesting that the dispersive Rossby waves that compose them undergo constructive and destructive interference as the flow evolves. In contrast, the coherency of the high-amplitude case suggests that nonlinear effects balance the dispersion (*36*).

In our high-amplitude runs, the hot spots tend to adopt a preferred size. Hot spots that begin too long or too short converge over the span of a few weeks to about 15,000 to 20,000 km. Real hot spots range in length from 5000 to 10,000 km (*15, 16, 37*). Their smaller size may result from a higher Δp_0 than is achieved in our simulations, because smaller features are composed of a greater range of wavenumbers and require stronger nonlinear effects to counteract the greater wave dispersion.

Several nonlinear effects may play a role in our simulations. When nominal Δp_0 is used, the air equatorward of 6° latitude undergoes latitudinal excursions of ~2° to 6° (Fig. 3), which causes large latitudinal variation of eastward wind as the air changes its distance from Jupiter's rotational axis. This results in a slow wind speed of 40 to 50 m s^{-1} within 3° of the equator (as compared to 85 m s^{-1} near the equator in simulations with one-tenth nominal Δp_0) that may contribute to the slower eastward propagation speeds of the hot spots initialized at nominal Δp_0 relative to those initialized with lower Δp_0. Furthermore, the large latitudinal excursions lead to an equatorial strip of nearly constant potential vorticity that may play a role in trapping hot spots to one hemisphere, because Rossby waves cannot propagate through regions of constant potential vorticity. Rossby wave behavior is also affected by the value and latitudinal profile of the potential vorticity gradient, which is different in our high-amplitude case because of the strong eddy perturbations induced by the hot spots. Finally, the Brunt-Vaisala frequency drops to about 0.0037 s^{-1} inside hot spots in the simulations with nominal Δp_0 (from its initial value of 0.005 s^{-1}) because of the downward stretching process. This effect alters the dynamics relative to the case with one-tenth nominal Δp_0, where the Brunt-Vaisala frequency remains nearly constant at 0.005 s^{-1} everywhere. The nonlinear advective term itself, however, is generally not more than 20% of the magnitude of the Coriolis and pressure-gradient terms even in our highest amplitude simulations, implying that the dominant force balance is still largely geostrophic after the initial adjustment is complete.

We varied λ_0 of hot spots in some simulations to test the sensitivity to horizontal shear and to changes in the Coriolis acceleration. Pressure anomalies with nominal Δp_0 placed at the equator evolved into coherent structures that propagate eastward at 100 m s^{-1} relative to the equatorial jet and have roughly three times smaller meridional winds than the simulations described above. We identify these as equatorial Kelvin waves. Pressure anomalies with one-third nominal Δp_0 placed at 32°N dispersed and did not produce coherent structures, whereas those placed at 16°N generated weak coherent structures that advect with the flow and contain closed contours of potential vorticity, suggesting that they are vortices.

Our simulations help to explain Jupiter's equatorial plumes, which are 10,000-km-long wedges of high cloud opacity that exist between hot spots. The dark regions on the equator in Fig. 2 are locations where air has been lifted to 1.5 bars from an initial pressure of 2 to 3 bars and would correspond to regions of cloud formation. The horizontal position of these features is where equatorial plumes occur relative to the hot spots. Air moves through the features from west to east, undergoing an oscillation in both latitude and height that takes it from the dark regions (plumes) to the bright regions (hot spots) in a few days.

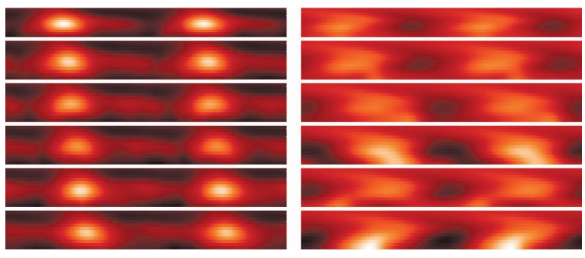

Fig. 4. Comparison of hot spot morphology versus time at high and low amplitudes (left and right columns, which were initalized with nominal and one-tenth nominal Δp_0, respectively) in two otherwise identical simulations. Each strip extends 120° in longitude and 4° to 13°N in latitude. Time increases downwards at 22-hour intervals, beginning at 55 days. Shown is pressure on a 165 K isentrope as in the previous figures. From dark to light, the orange scale spans 1.8 to 3.3 bars on the left and 1.72 to 1.9 bars on the right. These results argue against a linear-wave interpretation for hot spots.

References and Notes

1. Solar composition is defined as the solar O/H, S/H, and N/H molar ratios with the oxygen, sulfur, and nitrogen speciated into water, H_2S, and NH_3, as expected in Jupiter's troposphere.
2. H. B. Niemann *et al.*, *J. Geophys. Res.* **103**, 22831 (1998).
3. W. M. Folkner, R. Woo, S. Nandi, *J. Geophys. Res.* **103**, 22847 (1998).
4. P. R. Mahaffy, H. B. Niemann, J. E. Demick, *Bull. Am. Astron. Soc.* **31**, 1154 (1999).
5. J. B. Pollack and P. Bodenheimer, in *Origin and Evolution of Planetary and Satellite Atmospheres* (Univ. of Arizona Press, Tucson, AZ, 1989), pp. 564–602.
6. T. Guillot, *Science* **286**, 72 (1999).
7. S. K. Atreya *et al.*, *Planet. Space Sci.* **47**, 1243 (1999).
8. T. Owen *et al.*, *Nature* **402**, 269 (1999).
9. B. E. Carlson, A. A. Lacis, W. B. Rossow, *Astrophys. J.* **388**, 648 (1992).
10. A. P. Ingersoll and H. Kanamori, *Nature* **374**, 706 (1995).
11. M. Allison, *Icarus* **83**, 282 (1990).
12. F. M. Flasar and P. J. Gierasch, *J. Atmos. Sci.* **43**, 2683 (1986).
13. D. H. Atkinson, J. B. Pollack, A. Seiff, *J. Geophys. Res.* **103**, 22911 (1998).
14. T. E. Dowling, *Icarus* **117**, 439 (1995).
15. G. S. Orton *et al.*, *J. Geophys. Res.* **103**, 22791 (1998).
16. J. L. Ortiz *et al.*, *J. Geophys. Res.* **103**, 23051 (1998).

17. G. L. Bjoraker, H. P. Larson, V. G. Kunde, *Astrophys. J.* **311**, 1058 (1986).
18. B. E. Carlson, A. A. Lacis, W. B. Rossow, *J. Geophys. Res.* **99**, 14623 (1994).
19. M. Roos-Serote *et al.*, *J. Geophys. Res.* **103**, 23023 (1998).
20. P. G. J. Irwin *et al.*, *J. Geophys. Res.* **103**, 23001 (1998).
21. T. C. Owen *et al.*, *Eos* (Spring Suppl.) **77**, S171 (1996).
22. S. Atreya, M. H. Wong, T. Owen, H. Niemann, P. Mahaffy, in *Three Galileos: The Man, the Spacecraft, the Telescope* (proceedings of conference held 7 to 10 January 1997, Padova, Italy), J. Rahe, C. Barbieri, T. Johnson, A. Sohus, Eds. (Kluwer Academic, Dordrecht, Netherlands, 1997).
23. A. P. Showman and A. P. Ingersoll, *Icarus* **132**, 205 (1998).
24. R. D. Baker and G. Schubert, *Icarus* **136**, 340 (1998).
25. T. E. Dowling *et al.*, *Icarus* **132**, 221 (1998).
26. S. S. Limaye, *Icarus* **65**, 335 (1986).
27. The Brunt-Vaisala frequency, defined as the oscillation frequency for a vertically displaced air parcel, measures the atmosphere's static stability. On Earth and probably Jupiter, latent heat release in thunderstorms leads to a tropospheric temperature profile that decreases with height more slowly than the dry adiabatic profile and is hence stable to small-scale convection. For Jupiter, the dry adiabatic temperature gradient is –1.8 K km^{-1} whereas that with a Brunt-Vaisala frequency of 0.005 s^{-1} is –1.5 K km^{-1}.
28. We place the model bottom near 5 bars because latent heat effects are expected to generate a stable layer starting at about that altitude. The model assumes an ideal gas with a specific heat at constant pressure of 12,250 J kg^{-1} K^{-1} and gas constant of 3,500 J kg^{-1} K^{-1}. To verify that our results are independent of the boundary conditions, we performed some simulations with domains extending 360° in longitude or pole-to-pole in latitude.
29. The hyperviscosity is a high-order diffusion applied to all the dynamical variables and is typically ∇^4 for the first 30 Earth days of simulation and ∇^6 for subsequent times, with coefficients equal to half the upper limits from (*25*). The radiation is a Newtonian cooling that linearly relaxes temperature to an assumed equilibrium profile. The "sponge" is a Rayleigh drag, i.e., a linear relaxation of the winds to the assumed initial winds [from (*26*)], applied to the uppermost layers. These are all discussed extensively in (*25*).
30. The value of *a* is adjusted with the number of hot spots (generally 28°, 14°, 9°, and 6° longitude for 1, 2, 3, and 5 hot spots, respectively). The value of *b* is generally kept fixed at 4° latitude. We do not dynamically balance the winds inside the pressure anomalies. The model therefore undergoes a violent dynamical adjustment that lasts about 10 days. To prevent the adjustment phase from altering our results, we perform analysis only at times exceeding 50 days.
31. Hot spots are confined to 6° to 8°N latitude and have no counterpart in the southern hemisphere (*16*). Observations occasionally show equatorial plumes (10^4-km wedge-shaped clouds that are dynamically connected to hot spots) in the southern as well as northern hemisphere (*11*), however, suggesting that the confinement to a single hemisphere is not complete. Furthermore, ground-based observations before 1910 show plumes and dark features (presumably hot spots) in the southern rather than northern hemisphere, suggesting that long-period oscillations of hot spots between hemispheres may be possible.
32. Ground-based microwave observations show that ammonia is approximately 1 to 1.5 times solar from 2 to 5 bars over much of the planet (*7*). If NH_3 abundances of ~3 times solar are confined below 5 bars outside hot spots, then air parcels need only undergo pressure increases of twofold or less when entering hot spots to explain the probe ammonia observations, as opposed to the eightfold pressure increases indicated by comparison of equilibrium condensation models with probe data. To explain probe water measurements, however, the higher amplitudes may still be needed for parcels that enter hot spots deeper than 5 bars, unless (outside hot spots) water is confined to altitudes substantially below the condensation region in a manner analogous to that observed for ammonia.
33. R. F. Beebe, G. S. Orton, R. A. West, in *Time-Variable Phenomena in the Jovian System*, M. J. S. Belton, R. A. West, J. Rahe, Eds., NASA Spec. Publ. 494 (1989), pp. 245–288.
34. R. F. Beebe, A. A. Simon, L. F. Huber, *Science* **272**, 841 (1996).
35. A. J. Friedson and G. S. Orton, *Bull. Am. Astron. Soc.* **31**, 1155 (1999).
36. J. P. Boyd, in *Proceedings of the International School of Physics "Enrico Fermi" Course CIX: Nonlinear Topics in Ocean Physics* (North-Holland, New York, 1991), pp. 51–97.
37. A. R. Vasavada *et al.*, *Icarus* **135**, 265 (1998).
38. This research was supported by NASA and the NRC. We gratefully acknowledge numerous discussions with R. E. Young, J. Y-K. Cho, and A. P. Ingersoll.

20 April 2000; accepted 13 July 2000

Altered River Morphology in South Africa Related to the Permian-Triassic Extinction

Peter D. Ward,[1]* David R. Montgomery,[1] Roger Smith[2]

The Permian-Triassic transition in the Karoo Basin of South Africa was characterized by a rapid and apparently basin-wide change from meandering to braided river systems, as evidenced by preserved sedimentary facies. This radical changeover in river morphology is consistent with geomorphic consequences stemming from a rapid and major die-off of rooted plant life in the basin. Evidence from correlative nonmarine strata elsewhere in the world containing fluvial Permian-Triassic boundary sections suggests that a catastrophic terrestrial die-off of vegetation was a global event, producing a marked increase in sediment yield as well as contributing to the global $\delta^{13}C$ excursion across the Permian-Triassic boundary.

The Permian-Triassic (P-T) mass extinction killed more than 90% of marine species and about 70% of terrestrial vertebrate families (*1*). Several causes for the P-T extinction have been proposed, including an asteroid or comet impact (*2*), environmental change (*3, 4*), oceanic anoxia (*5*) or overturn (*6*), volcanism (*7, 8*), and synergistic combinations of these possible causes (*9*). Less is known about the extinctions on land than those in the sea. Perhaps the best studied record of vertebrate taxa across the P-T boundary is found in the Karoo Basin of South Africa, which records a complete stratigraphic record of Permian through Triassic systems in the interior of southern Pangaea and contains well-exposed P-T boundary sections with relatively abundant vertebrate fossils. The P-T boundaries in the Karoo can be correlated with marine P-T stratotypes using carbon isotope stratigraphy (*10*), which also indirectly dates the P-T boundary in the Karoo at about 251 million years ago (Ma) (*11*).

The record of vertebrate survivorship in the Karoo Basin is relatively well known. Only 6 of the 44 reptilian genera recovered to date from the highest Permian biostratigraphic zone (*Dicynodon* assemblage zone) are also found in the succeeding *Lystrosaurus* assemblage zone (*12*). The fossil record of Permian plants is less complete from the Karoo because of diagenesis, but correlative strata from other stratigraphic sections of Gondwanaland record a major floral extinction pulse at the boundary (*13*). The rapidity and cause of the extinctions among terrestrial organisms in the Karoo remains controversial, with claims of long-term (10^6 years) climate change (*14*) or more rapid (10^4 years) causes (*4*). In the latter study, the change of fluvial style, with concomitant changes in plant ecosystems, was suggested to be the cause of the vertebrate extinction in the basin. The proximal cause of this environmental change was thought to be a major pulse of tectonic activity along the southern margin of the Karoo, causing uplift in the basin (*4*).

We measured stratigraphic sections across seven P-T boundary localities scattered across 400 km of the Karoo Basin (*15*). These sections show similar changes in facies across the P-T boundary (Fig. 1). Three distinct facies associations were determined. Below the boundary, sandstone bodies show an association of sedimentary facies that are consistent with formation by scour and sedimentation in a confined unidirectional flow, such as is produced by large meandering rivers of high sinuosity. These meandering channel sandstones are commonly single-storied and are characterized by low-angle (20° to 25°) lateral accretion surfaces that extend throughout the thickness of the channel sandstone and into the overlying channel bank deposits as interdigitating sandstone string-

[1]Department of Geological Sciences, University of Washington, Seattle, WA 98195, USA. [2]South African Museum, Cape Town, South Africa.

*To whom correspondence should be addressed.